

# Nanowires of Methylammonium Lead Iodide ( $\text{CH}_3\text{NH}_3\text{PbI}_3$ ) Prepared by Low Temperature Solution-Mediated Crystallization

Endre Horváth,<sup>\*,†</sup> Massimo Spina,<sup>†</sup> Zsolt Szekrényes,<sup>‡</sup> Katalin Kamarás,<sup>‡</sup> Richard Gaal,<sup>†</sup> David Gachet,<sup>§</sup> and László Forró<sup>†</sup>

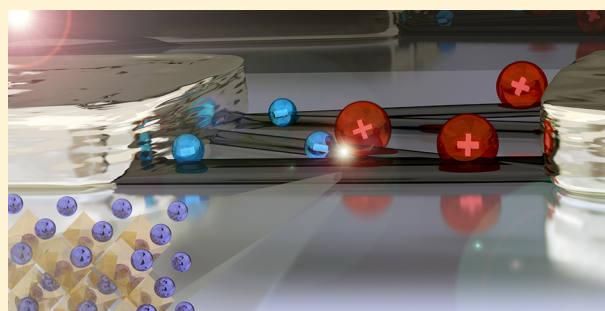
<sup>†</sup>Laboratory of Physics of Complex Matter (LPMC), Ecole Polytechnique Fédérale de Lausanne, 1015 Lausanne, Switzerland

<sup>‡</sup>Institute for Solid State Physics and Optics, Wigner Research Centre for Physics, Hungarian Academy of Sciences, 1525 Budapest, Hungary

<sup>§</sup>Attolight AG, Innovation Park, 1015 Lausanne, Switzerland

## S Supporting Information

**ABSTRACT:** We report the synthesis of Methylammonium Lead Iodide ( $\text{CH}_3\text{NH}_3\text{PbI}_3$ ) nanowires by a low temperature solution processed crystallization using a simple slip-coating method. The anisotropic particle shape exhibits advantages over nanoparticles in terms of charge transport under illumination. These results provide a basis for solvent-mediated tailoring of structural properties like the crystallite size and orientation in trihalide perovskite thin films, which, once implemented into a device, may ultimately result in an enhanced charge carrier extraction.



**KEYWORDS:** Perovskite, solar cell, photodetector, grain boundary, crystallization

Perovskites, the structural analogues of the natural crystal of calcium titanium oxide, cover a broad range of versatile materials, which have potential applications in multiple fields such as superconductors,<sup>1</sup> sensors,<sup>2</sup> fuel cells,<sup>3</sup> ferroelectrics<sup>4</sup> and thermoelectrics.<sup>5</sup> The recently rediscovered, half-century old members of this family,<sup>6</sup> organolead halide perovskites, turned out to be promising components of next generation solar cells.<sup>7</sup> Incorporated as light harvesters in mesoscopic solar cells, a remarkable power conversion efficiency of 16.2% was demonstrated in lab-scale devices.<sup>8</sup> It has been shown that aside from the role of the light absorber, the organolead halide perovskites can be viewed both as electron and hole transporting media due to their ambipolar charge transport character.<sup>9</sup> So far, the highest solar-to-electric conversions have been reached with two main compounds ( $\text{CH}_3\text{NH}_3\text{PbI}_3$  and  $\text{CH}_3\text{NH}_3\text{PbI}_{3-x}\text{Cl}_x$ , abbreviated as  $\text{MAPbI}_3$  and  $\text{MAPbI}_{3-x}\text{Cl}_x$ ) showing minor alterations in halide content.<sup>10,11</sup> These are direct band gap semiconductors with a high absorption coefficient, a favorable band gap of 1.5–1.65 eV and electron–hole diffusion length ranging from  $\approx 100$  nm to  $\approx 1$   $\mu\text{m}$ .<sup>12,8,13,14</sup> However, the structural and electronic differences between the two materials, as well as the exact role of the Cl anions have yet to be undoubtedly determined by the scientific community. Colella et al.<sup>15</sup> observed that incorporation of Cl as a dopant dramatically improves the charge transport within the perovskite layer. It has also been described that the Cl inclusion enhances the granular morphology resulting in a more homogeneous current production probed by electron beam-induced current (EBIC) method.<sup>16</sup> Very recently, by inserting

formamidinium cations into a lead iodide structure, nearly cubic phase (band gap  $\approx 1.43$  eV) perovskite was reported, with an absorption edge broadened by 30 nm as compared to  $\text{MAPbI}_3$ .<sup>17</sup> These findings validate the bandgap engineering strategies, where the bandgap of the material might be efficiently tuned by choosing the halide anion and the organic amide constituent.<sup>18–20</sup> One of the key aspects toward a low-cost technology capable of competing with the established silicon technology lies in the material's low temperature solution processability. The current approach is based on a single step deposition of a mixture of  $\text{PbX}_2$  and  $\text{CH}_3\text{NH}_3\text{X}$  (X is a halide anion) in a common solvent or sequential deposition of the constituents from a solution onto a mesoporous scaffold.<sup>21,22</sup> Rapid crystallization of the perovskite has been observed during the spin-coating process. To obtain an optimized device performance, very often a postannealing treatment is required. Recent results<sup>23</sup> demonstrated an efficiency of 15% on devices entirely processed below 150 °C. The general observation is that minor alterations of the applied processing parameters may lead to dramatically different device performances. This indicates that it is critical to have fine control over the nucleation and crystal growth of the  $\text{MAPbI}_3$ . In their effort to control the morphology of the trihalide perovskite films, Eperon et al.<sup>24</sup> showed that the

Received: June 3, 2014

Revised: September 12, 2014

Published: October 29, 2014



highest photocurrents were attainable only with the highest perovskite surface coverage. This prior work suggests that the final crystalline morphology depends mainly on the dynamics of annealing, which will ultimately govern the solvent evaporation, pore voiding or closing and the film thickness. Liu and co-workers reported<sup>25</sup> that the solution-cast films onto a compact TiO<sub>2</sub>-layer over an FTO-coated glass inhomogeneously covered the substrate and that it was composed of crystalline “platelets” with a length on the scale of tens of micrometres. The crystallite sizes determined from X-ray diffraction were larger than 400 nm. On the other hand, studies based on electron microscopy observations report the presence of small, ~6 nm nanoparticles supported by surface-modified mesoporous TiO<sub>2</sub> film prepared by solution processing.<sup>26</sup> As is well-known, the dimensionality and morphology of crystallites may have a striking influence on their chemical and physical properties. Under most circumstances, nano- and micrometer-sized particles with isotropic particle shapes have been observed. This suggests that the crystallites tend to grow uniformly along the three major crystallographic directions. This can be easily accepted, since MAPbI<sub>3</sub> more likely crystallizes in a cubic structure, therefore in principle there should be no crystallographic driving force for anisotropic growth. Surprisingly, we found that some solvents induce highly anisotropic crystallization of MAPbI<sub>3</sub>. To the authors’ knowledge, no 1D form of organolead halide perovskites has been observed to date.

Here we report the synthesis of two sets of MAPbI<sub>3</sub> nanowires with mean diameter of 50 and 400 nm and length up to 10 μm. They were prepared through a simple slip-coating approach. The one-dimensional form of MAPbI<sub>3</sub> could have unique optical and electrical properties. The feasibility of anisotropic growth of organolead halide perovskites opens up a new strategy toward the realization of low-temperature, solution processed films with controlled morphology.

**Synthesis.** Saturated solution of MAPbI<sub>3</sub> in dimethylformamide (DMF) was dropped onto a glass microscope slide and covered with a second glass slide so that the excess yellow solution squeezed out; the remaining solution formed a homogeneous liquid film between the glass plates (Figure 1a–c, details of the synthesis can be found in the Supporting Information). The excess of MAPbI<sub>3</sub> solution was removed from the sides by soaking with a tissue. Next, the bottom substrate was held in place while gradually sliding the upper glass plate, exposing the thin liquid film to air. Solvent evaporation from the uncovered surface caused an instantaneous yellow to brown-red color change.

Optical microscopy was performed to confirm the crystallization of the solid. Unexpectedly, instead of a granular film composed of isotropic crystallites, a network of several micron long wire-like objects was observed, some of them pointing in the direction of sliding of the two glass plates (Figure 1d,e). The filiform morphology was further confirmed using TEM, SEM and AFM measurements.

The width of the nanowires varied between 50 and 200 nm, and they had lengths up to 16 μm. The height of the crystallites was determined from AFM measurements displaying a range from ultrathin (~9 nm) to several tens of nanometers thick (~90 nm) scale. The formation of a small number of aggregates of ~10 nm sized isotropic crystallites was also observed, as can be seen on TEM and SEM micrographs (Figure 2a,b). These particles were homogeneously dispersed on the SiO<sub>2</sub> surface and attached to the wall of larger nanowires (Figure 2b).

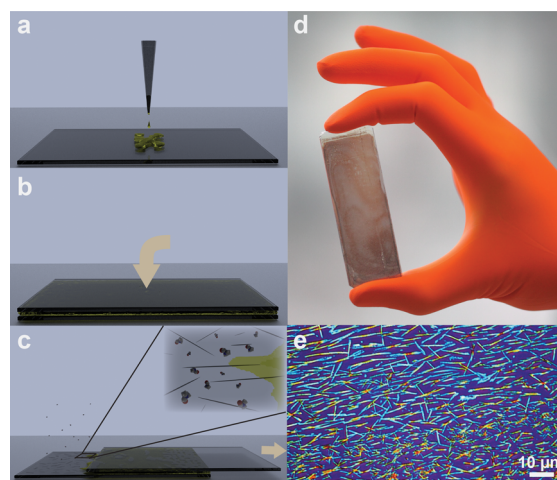


**Figure 1.** Schematic illustration of the low temperature slip-coating process for the fabrication of filiform lead-methylamine iodide perovskite thin films (a–c). Photo of the coating formed on a microscope glass slide (d). Optical microscopy image of filiform crystallites grown on SiO<sub>2</sub>/Si substrate (e).

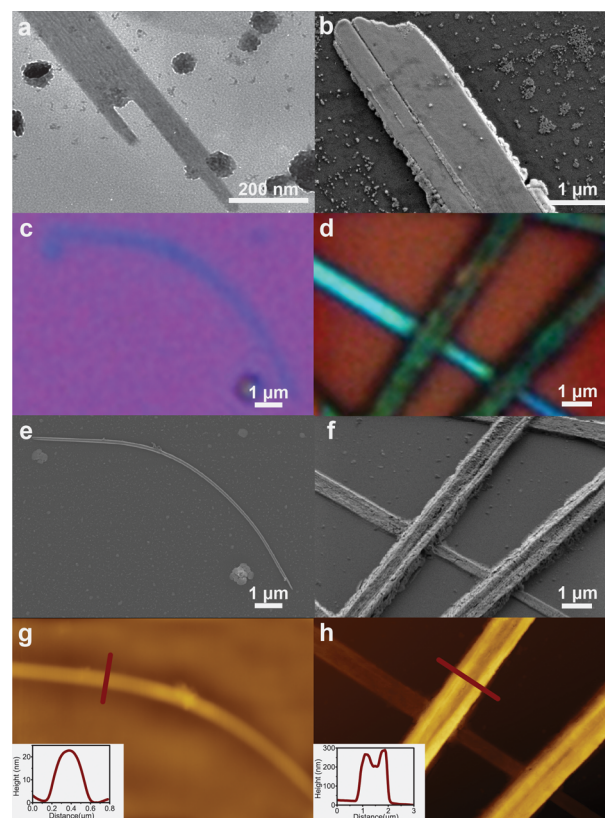


**Figure 2.** Morphological parameters of filiform MAPbI<sub>3</sub> crystallites. TEM image of a MAPbI<sub>3</sub> (a). Optical microscope images of individual MAPbI<sub>3</sub> nanowire (c and d). SEM image of micrometer-sized MAPbI<sub>3</sub> filaments grown on SiO<sub>2</sub>/Si surface (b, e, and f). AFM images and height profiles. The white lines denote the corresponding cross-sectional profiles shown in the insets (g and h). Note that for panels c–g and d–h, the same zones of the surfaces are imaged.

Increasing the MAPbI<sub>3</sub> solution volume-to-surface ratio during the slip-coating process yields larger, submicrometer sized whiskers (Figure 2b,d,f,h, experimental details in the Supporting Information). Unlike the thinner wires that have a flat

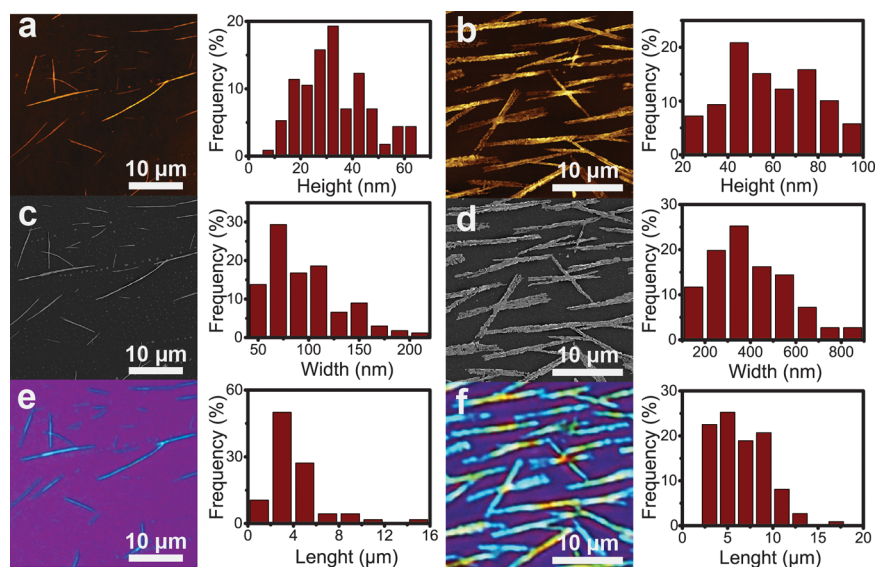


**Figure 3.** Size distribution of two sets of nanowires of MAPbI<sub>3</sub>. The height has been determined by AFM (a and b), while the width and length have been obtained by SEM (c and d) and optical microscopy (e and f) images.

surface, some of these thicker crystallites possess a U-shape void along their surface. The size distribution of nanowires (read from optical, AFM and SEM images) prepared by two solution volumes is shown in Figure 3. We experienced that parameters such as solvent concentration, temperature, fluid philicity/phobicity, sliding speed, etc. influence the kinetics of crystallization. We assume that the optimized combination of these parameters could result in a major product having well-controlled surface density, crystal habit, aspect ratio, size-distribution and even orientation on a given substrate.

The elemental composition of the anisotropic crystallites was analyzed by EDX. The presence of lead and iodine was readily confirmed, while the low atomic number carbon and nitrogen cannot be reliably quantified by EDX (Supporting Information Figure S3). The Pb:I atomic percent ratio was found to be 25:75. To gain more insight into the structure of the nanowires XRD, Raman and infrared spectroscopies were performed. The XRD diffractogram shows high intensity diffraction peaks at  $2\theta$  14° (110) and 28.4° (220), which were identified as the characteristic peaks of the cubic MAPbI<sub>3</sub> phase.<sup>27</sup> The presence of the low intensity peak at 12.54° is assigned to a PbI<sub>2</sub> phase which presumably formed as a result of the humidity-induced partial decomposition of MAPbI<sub>3</sub> during the PXRD measurement. The presence of two major reflection peaks suggests that the crystallites are highly oriented along the (110) direction. Raman spectra recorded on filiform crystallites are also in accordance with the reported Raman modes of MAPbI<sub>3</sub>.<sup>28</sup> The cathodoluminescence spectrum of filiform nanoparticles shows a single peak centered at ~770 nm, ~1.61 eV (Supporting Information Figure S7). This peak position corresponds well with the band gap reported of MAPbI<sub>3</sub> perovskites (1.5–1.6 eV). Furthermore, Fourier Transform Infrared Spectroscopy (FTIR) spectra show a close correspondence in the vibration modes of filiform crystallites and bulk single crystal suggesting identical chemical composition (CH<sub>3</sub>NH<sub>3</sub>PbI<sub>3</sub>).

The central question is where does the directionality of the perovskite growth stem from? The role of the solvent in the nanowire formation was investigated by changing the solvent. The same protocol was repeated by replacing dimethylformamide (DMF) by  $\gamma$ -butyrolactone (GBL), another commonly

used solvent of organolead halide perovskites. Due to GBL's higher boiling point, the evaporation was much slower, and ca. 350 K heat treatment was required to evaporate the solvent. Clearly, no anisotropic growth was taking place during the slip-coating process from GBL solution. Thus, we assume that the use of DMF is the key step, and therefore, a unique role of DMF as a growth-directing agent is suggested. It is not clear yet whether DMF specifically affects the crystallization kinetics of the lead iodide framework or if the directional growth is due to an internal complex or adduct formation with the methylamine group. Currently, we are assuming the second as a working hypothesis. The elucidation of the exact role of DMF on the formation of different solvatomorphs will be the subject of further studies.

**Testing of Photoresponse of the Nanowires.** The major interest in MAPbI<sub>3</sub> is its high sensitivity to visible-light this together with its high photovoltage of about 1.1 V are the basic ingredients for efficient solar-to-electric energy conversion.<sup>29</sup> These advantageous characteristics will certainly be explored in other device-oriented research, like photodetection and solid state lasers.<sup>30</sup> The elucidation of the morphology-dependent photoconductive performance could have a consequence on the development of more efficient devices. So far, the intrinsic photoconductive properties measured by standard contact methods have not even been reported for the bulk samples. Here, we demonstrate the first results showing that one can make efficient photodetectors based on nanowires of MAPbI<sub>3</sub>. In addition, these findings are compared to the photodetection of a thin film of spin coated MAPbI<sub>3</sub> frequently used in photovoltaic devices.

The devices were fabricated by slip-coating nanowires of different sizes of MAPbI<sub>3</sub> onto a highly p-doped silicon substrate with 300 nm SiO<sub>2</sub> on top, and 100 nm-thick Pt contacts were deposited by e-beam evaporation through a microfabricated hard mask. The fabricated devices have a width of 100  $\mu$ m and a length varying between 5 and 50  $\mu$ m. The sketch and the optical image of a device are shown in Figure 4a,b.

We measured the current density in the device as a function of the applied source-to-drain electric field in the dark and

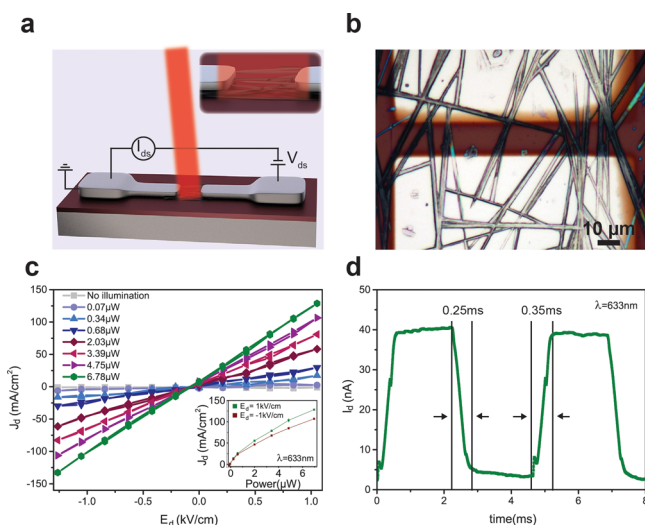


**Figure 4.** Schematic illustration of the nanowire-based device fabricated for FET and  $I$ - $V$  photocurrent measurements (a). Optical microscopy image showing the MAPbI<sub>3</sub> nanowires crossing the Pt source-drain contacts deposited by e-beam evaporation (b). Dark and laser illuminated  $I$ - $V$  curves under increasing laser power (c). Time-resolved photoresponse (d).

under illumination (red laser,  $\lambda = 633$  nm). The output characteristics follow a linear behavior, indicating that the contacts are ohmic (Figure 4c). (The contacts show a slight asymmetric behavior probably due to fabrication asymmetries.)

In the dark state, the device behaves like a good insulator with currents of the order of tens of pA and resistances in the GOhm range. Under the illumination of the laser, the absorption of the light generates electron-hole pairs that are extracted by the source-to-drain electric field and cause an increase in the conductance of the material up to a factor of 300. We probed the photoresponse of the device under different incident laser powers in the 70 nW to 7  $\mu$ W range. The current increases parabolically with the incident power, however, under the applied experimental conditions the saturation of the photocurrent was not reached (inset to Figure 4c).

The device configuration allows to test the effect of a gate electric field on the  $I$ - $V$  characteristics. Despite the semi-conducting nature of the material, no influence of gating was noticed (Supporting Information Figure S12). The applicable electric field limit (breakdown voltage) was determined to be  $\approx 20$  kV/cm. Higher electric fields risk an irreversible rupture of the filiform crystallites (Supporting Information Figure S13).

From the photocurrent, one can estimate the responsivity of the device defined as  $R = I_{ph}/P_{in}$ , where  $I_{ph}$  is the photocurrent and  $P_{in}$  is the power of the incident light. For our device,  $R$  was calculated to be 5 mA/W. Although this value is about 4 orders of magnitude smaller than the best-in-class photoelectric devices made out of graphene and monolayer MoS<sub>2</sub>,<sup>31–34</sup> it is still comparable (10 times higher) to the value that has been achieved with the first prototypes of those 2D materials<sup>35,36</sup> (Supporting Information Chart S1). Optimization of the device fabrication process and the engineering of its configuration might improve the performances of the photodetectors based on filiform perovskites.

The response time of our device (Figure 4d) showed that rise and decay times for the on-off current under illumination are less than 500  $\mu$ s,  $\sim 10^4$  faster than the state-of-the-art

photodetectors made of monolayer MoS<sub>2</sub><sup>31,33</sup> and graphene.<sup>32,34,37</sup> The stability of the device was also tested by performing  $\sim 100$  consecutive cycles measured over 1 h (Supporting Information Figure S14). A slight increase of the photocurrent ( $\sim 5\%$ ) over time is presumably due to contact adjustments (a better interface is created with the metal trough some annealing mechanism, Supporting Information Figure S14). In recent studies, several groups<sup>38–40</sup> working on perovskite-based solar cells have reported a slight increase of  $J_{sc}$  (short-circuit current) after sequential measurements of light conversion efficiency or in the first hours of light instability tests. It has been suggested that the slight increase of the photocurrent could be the result of ionic charge transport, ion intercalation, or it might even be a ferroelectric effect. Deeper electrical and electro-optical characterization is needed to establish the exact mechanisms.

To compare the performance of the wire structure (Figure 5a, upper panel) with respect to the spin-coated film used today

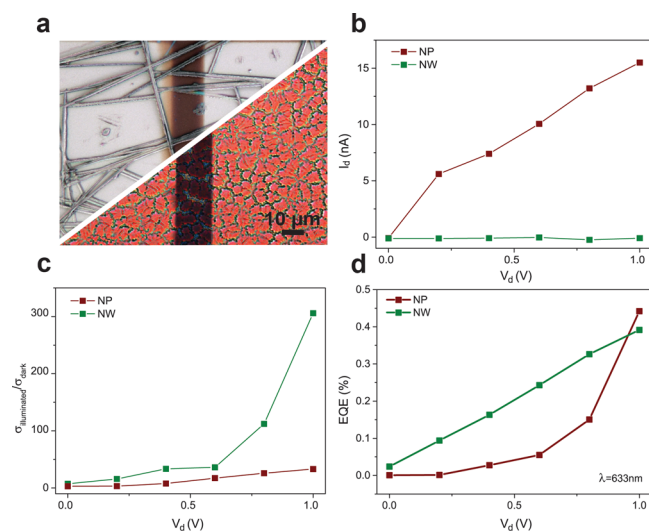


**Figure 5.** (a) Combined SEM-optical micrographs showing the surface of the thin film composed of nearly isotropic MAPbI<sub>3</sub> particles (bottom) and nanowires (top) with the Pt source-drain contacts deposited by e-beam evaporation (a). The grain boundaries in the nanoparticle-based film are clearly perceivable with a green-blue color (a, bottom). Note the absence of such a contrast in the case of filiform perovskites (a, top). Comparison of the dark current density of the nanoparticle and nanowire based devices (b). Comparison of the photocurrent-dark current ratio of the nanoparticle and nanowire based devices (c). Comparison of the external quantum efficiency of the nanoparticle and nanowire based devices (d).

in solar cells, a photodetector with a film of MAPbI<sub>3</sub> nanoparticles was produced (Figure 5a, lower panel). Figure 5b gives the current density (calculated with the corresponding geometrical factors, details are in the Supporting Information) as a function of the source-drain voltage. The dark current measurements revealed that the flow of charge carriers is facilitated in the coating composed of MAPbI<sub>3</sub> nanoparticles slip-coated from GBL solution. The photocurrent-dark current ratio under a laser intensity of 2.5 Wcm<sup>-2</sup> ( $\lambda = 633$  nm) increases exponentially for the elongated perovskites, while the increase is almost linear for the nanoparticles (Figure 5c). The photocurrent-dark current ratio is 1 order of magnitude higher for filiform crystallites applying 1 kV/cm electric field. The performance limitations in the nanoparticle based film (most

probably due to the increased number of grain boundaries) are also observable from the external quantum efficiency (EQE) defined as  $R_{hw}/e$  (details are in Supporting Information). For low voltages (<0.5 V), the EQE of the device made of fibrous perovskites is twice as high as the photodetector prepared from MAPbI<sub>3</sub> nanoparticles.

These results demonstrate that the morphological properties, such as the crystallite size, form, and its orientation, could play an essential role in the photodetection and photoconductive response of the trihalide perovskite thin films.

**Conclusion.** Methylammonium Lead Iodide in a photo-voltaic configuration with a very simple processing has already demonstrated 16% light conversion efficiency. We hypothesize that improving the materials properties could increase the upper limits of this conversion. Keeping in mind dye-sensitized solar cells with solid state electrolyte, where the replacement of TiO<sub>2</sub> nanoparticles with nanowires has considerably improved efficiency, we have developed the synthesis of MAPbI<sub>3</sub> nanowires. Their transport (photophysical) characteristics supersede those of isotropic nanocrystal-based thin films used in current devices. The relevant example, that recrystallization from solvents of different nature facilitates the formation of elongated solvatomorphs of Methylammonium Lead Iodide, gives an opportunity to realize new solution-mediated strategies with the ultimate goal of exerting control over crystallite characteristics. The optically active elongated form of trihalide perovskites will make it possible to explore exciting opportunities in the photonics industry such as solar energy conversion, photodetectors, light-emitting diodes, and on-chip coherent light sources.

## ■ ASSOCIATED CONTENT

### ■ Supporting Information

Details of syntheses; experimental details; material characterization; device fabrication, characterization, and geometry calculations; effect of the gate voltage. This material is available free of charge via the Internet at <http://pubs.acs.org>.

## ■ AUTHOR INFORMATION

### Corresponding Author

\*E-mail: [endre.horvath@epfl.ch](mailto:endre.horvath@epfl.ch). Tel.: +41 21 69 34515. Fax: +41 21 693 4470.

### Notes

The authors declare no competing financial interest.

## ■ ACKNOWLEDGMENTS

This work was funded by the Swiss National Science Foundation and partially by the Hungarian Scientific Research Fund (OTKA) and the Austrian Science Fund (FWF) under Grant No. ANN 107580. We would like to thank Dr. Rosendo Sanjinez for his assistance with the current–voltage measurements. We acknowledge Dr. Eavan Dorsey for useful discussions. Device fabrication was carried out in part in the EPFL Center for Micro/Nanotechnology (CMI).

## ■ REFERENCES

- (1) He, T.; Huang, Q.; Ramirez, A. P.; Wang, Y.; Regan, K. A.; Rogado, N.; Hayward, M. A.; Haas, M. K.; Slusky, J. S.; Inumara, K.; Zandbergen, H. W.; Ong, N. P.; Cava, R. J. *Nature* **2001**, *411* (6833), 54–56.
- (2) Shimizu, Y.; Fukuyama, Y.; Arai, H.; Seiyama, T. Oxygen Sensor Using Perovskite-Type Oxides. In *Fundamentals and Applications of*

*Chemical Sensors*; American Chemical Society: Washington, DC, 1986; Vol. 309, pp 83–100.

- (3) Boukamp, B. A. *Nat. Mater.* **2003**, *2* (5), 294–296.
- (4) Pytte, E. *Phys. Rev. B* **1972**, *5* (9), 3758–3759.
- (5) Bocher, L.; Aguirre, M. H.; Logvinovich, D.; Shkabko, A.; Robert, R.; Trottmann, M.; Weidenkaff, A. *Inorg. Chem.* **2008**, *47* (18), 8077–8085.
- (6) Zhang, A.; Cheng, J.; Kim, H.; Liu, Y. S.; Lo, Y. H. *Quantum Sensing and Nanophotonic Devices VII* **2010**, 7608.
- (7) Kojima, A.; Teshima, K.; Shirai, Y.; Miyasaka, T. *J. Am. Chem. Soc.* **2009**, *131* (17), 6050–6051.
- (8) Liu, C.-H.; Chang, Y.-C.; Norris, T. B.; Zhong, Z. *Nat. Nanotechnol.* **2014**, *9* (4), 273–278.
- (9) Mosconi, E.; Amat, A.; Nazeeruddin, M. K.; Grätzel, M.; De Angelis, F. *J. Phys. Chem. C* **2013**, *117* (27), 13902–13913.
- (10) Kim, H.-S.; Lee, C.-R.; Im, J.-H.; Lee, K.-B.; Moehl, T.; Marchioro, A.; Moon, S.-J.; Humphry-Baker, R.; Yum, J.-H.; Moser, J. E.; Grätzel, M.; Park, N.-G. *Sci. Rep.* **2012**, *2*, 591.
- (11) Docampo, P.; Ball, J. M.; Darwich, M.; Eperon, G. E.; Snaith, H. *J. Nat. Commun.* **2013**, *4*, 2761.
- (12) Xing, G.; Mathews, N.; Sun, S.; Lim, S. S.; Lam, Y. M.; Grätzel, M.; Mhaisalkar, S.; Sum, T. C. *Science* **2013**, *342* (6156), 344–347.
- (13) Im, J.-H.; Lee, C.-R.; Lee, J.-W.; Park, S.-W.; Park, N.-G. *Nanoscale* **2011**, *3* (10), 4088–4093.
- (14) Stranks, S. D.; Eperon, G. E.; Grancini, G.; Menelaou, C.; Alcocer, M. J. P.; Leijtens, T.; Herz, L. M.; Petrozza, A.; Snaith, H. J. *Science* **2013**, *342* (6156), 341–344.
- (15) Colella, S.; Mosconi, E.; Fedeli, P.; Listorti, A.; Gazza, F.; Orlandi, F.; Ferro, P.; Besagni, T.; Rizzo, A.; Calestani, G.; Gigli, G.; De Angelis, F.; Mosca, R. *Chem. Mater.* **2013**, *25* (22), 4613–4618.
- (16) Edri, E.; Kirmayer, S.; Henning, A.; Mukhopadhyay, S.; Gartsman, K.; Rosenwaks, Y.; Hodes, G.; Cahen, D. *Nano Lett.* **2014**, *14* (2), 1000–1004.
- (17) Pang, S.; Hu, H.; Zhang, J.; Lv, S.; Yu, Y.; Wei, F.; Qin, T.; Xu, H.; Liu, Z.; Cui, G. *Chem. Mater.* **2014**, *26* (3), 1485–1491.
- (18) Noh, J. H.; Im, S. H.; Heo, J. H.; Mandal, T. N.; Seok, S. I. *Nano Lett.* **2013**, *13* (4), 1764–1769.
- (19) Kulkarni, S. A.; Baikie, T.; Boix, P. P.; Yantara, N.; Mathews, N.; Mhaisalkar, S. G. *J. Mater. Chem. A* **2014**, *2*, 9121–9225.
- (20) Im, J.-H.; Chung, J.; Kim, S.-J.; Park, N.-G. *Nanoscale Res. Lett.* **2012**, *7* (1), 353.
- (21) Ball, J. M.; Lee, M. M.; Hey, A.; Snaith, H. J. *Energy Environ. Sci.* **2013**, *6* (6), 1739–1743.
- (22) Burschka, J.; Pellet, N.; Moon, S.-J.; Humphry-Baker, R.; Gao, P.; Nazeeruddin, M. K.; Grätzel, M. *Nature* **2013**, *499* (7458), 316–319.
- (23) Wojciechowski, K.; Saliba, M.; Leijtens, T.; Abate, A.; Snaith, H. J. *Energy Environ. Sci.* **2014**, *7* (3), 1142–1147.
- (24) Eperon, G. E.; Burlakov, V. M.; Docampo, P.; Goriely, A.; Snaith, H. J. *Adv. Funct. Mater.* **2014**, *24* (1), 151–157.
- (25) Liu, M.; Johnston, M. B.; Snaith, H. J. *Nature* **2013**, *501* (7467), 395–398.
- (26) Qin, P.; Domanski, A. L.; Chandiran, A. K.; Berger, R.; Butt, H.-J.; Dar, M. I.; Moehl, T.; Tetreault, N.; Gao, P.; Ahmad, S.; Nazeeruddin, M. K.; Grätzel, M. *Nanoscale* **2014**, *6* (3), 1508–1514.
- (27) Baikie, T.; Fang, Y.; Kadro, J. M.; Schreyer, M.; Wei, F.; Mhaisalkar, S. G.; Graetzel, M.; White, T. J. *J. Mater. Chem. A* **2013**, *1* (18), 5628–5641.
- (28) Quarti, C.; Grancini, G.; Mosconi, E.; Bruno, P.; Ball, J. M.; Lee, M. M.; Snaith, H. J.; Petrozza, A.; Angelis, F. D. *J. Phys. Chem. Lett.* **2013**, *5* (2), 279–284.
- (29) Lee, M. M.; Teuscher, J.; Miyasaka, T.; Murakami, T. N.; Snaith, H. J. *Science* **2012**, *338* (6107), 643–647.
- (30) Xing, G.; Mathews, N.; Lim, S. S.; Yantara, N.; Liu, X.; Sabba, D.; Grätzel, M.; Mhaisalkar, S.; Sum, T. C. *Nat. Mater.* **2014**, *13*, 476–480.
- (31) Zhang, W. J.; Chuu, C. P.; Huang, J. K.; Chen, C. H.; Tsai, M. L.; Chang, Y. H.; Liang, C. T.; Chen, Y. Z.; Chueh, Y. L.; He, J. H.; Chou, M. Y.; Li, L. J. *Sci. Rep.* **2014**, *4*, 3826.

- (32) Jin, W.; Gao, Z.; Zhou, Y.; Yu, B.; Zhang, H.; Peng, H.; Liu, Z.; Dai, L. *J. Mater. Chem. C* **2014**, *2* (9), 1592–1596.
- (33) Lopez-Sanchez, O.; Lembke, D.; Kayci, M.; Radenovic, A.; Kis, A. *Nat. Nanotechnol.* **2013**, *8* (7), 497–501.
- (34) Konstantatos, G.; Badioli, M.; Gaudreau, L.; Osmond, J.; Bernechea, M.; de Arquer, F. P. G.; Gatti, F.; Koppens, F. H. L. *Nat. Nanotechnol.* **2012**, *7* (6), 363–368.
- (35) Xia, F. N.; Mueller, T.; Lin, Y. M.; Valdes-Garcia, A.; Avouris, P. *Nat. Nanotechnol.* **2009**, *4* (12), 839–843.
- (36) Yin, Z. Y.; Li, H.; Li, H.; Jiang, L.; Shi, Y. M.; Sun, Y. H.; Lu, G.; Zhang, Q.; Chen, X. D.; Zhang, H. *ACS Nano* **2012**, *6* (1), 74–80.
- (37) Zhang, Y. Z.; Liu, T.; Meng, B.; Li, X. H.; Liang, G. Z.; Hu, X. N.; Wang, Q. J. *Nat. Commun.* **2013**, *4*, 1811.
- (38) Dualeh, A.; Moehl, T.; Tétreault, N.; Teuscher, J.; Gao, P.; Nazeeruddin, M. K.; Grätzel, M. *ACS Nano* **2013**, *8* (1), 362–373.
- (39) Sanchez, R. S.; Gonzalez-Pedro, V.; Lee, J.-W.; Park, N.-G.; Kang, Y. S.; Mora-Sero, L.; Bisquert, J. *J. Phys. Chem. Lett.* **2014**, *5* (13), 2357–2363.
- (40) Leijtens, T.; Eperon, G. E.; Pathak, S.; Abate, A.; Lee, M. M.; Snaith, H. J. *Nat. Commun.* **2013**, *4*, 2885.